

Sensitivity of short-range order prediction to machine learning potential formalisms: A case study on NbMoTaW high-entropy alloy

Dingyi Jin(金定毅), Guo Wei(魏国), and Haidong Wang(王海东)

Citatio: Chin. Phys. B, 2025, 34 (**9**): 096104. DOI: 10.1088/1674-1056/ae039a
http://cpb.iphy.ac.cn; http://iopscience.iop.org/cpb

What follows is a list of articles you may be interested in

Molecular dynamics study of primary radiation damage in TiVTa concentrated solid-solution alloy

Yong-Peng Zhao(赵永鹏), Yan-Kun Dou(豆艳坤), Xin-Fu He(贺新福), Han Cao(曹晗),Lin-Feng Wang(王林枫), Hui-Qiu Deng(邓辉球), and Wen Yang(杨文)
Chin. Phys. B, 2024, 33 (**3**): 036104. DOI: 10.1088/1674-1056/ad0146

Geometries and electronic structures of Zr_nCu(n =2-12) clusters: A joint machine-learning potential density functional theory investigation

Yizhi Wang(王一志), Xiuhua Cui(崔秀花), Jing Liu(刘静), Qun Jing(井群), Haiming Duan(段海明), and Haibin Cao(曹海宾)
Chin. Phys. B, 2024, 33 (**1**): 016109. DOI: 10.1088/1674-1056/acd5c2

Atomic simulations of primary irradiation damage in U-Mo-Xe system

Wen-Hong Ouyang(欧阳文泓), Jian-Bo Liu(刘剑波), Wen-Sheng Lai(赖文生),Jia-Hao Li(李家好), and Bai-Xin Liu(柳百新)
Chin. Phys. B, 2023, 32 (**3**): 036101. DOI: 10.1088/1674-1056/ac9366

Microstructure and hardening effect of pure tungsten and ZrO_2 strengthened tungsten under carbon ion irradiation at 700℃

Chun-Yang Luo(罗春阳), Bo Cui(崔博), Liu-Jie Xu(徐流杰), Le Zong(宗乐), Chuan Xu(徐川), En-Gang Fu(付恩刚), Xiao-Song Zhou(周晓松), Xing-Gui Long(龙兴贵), Shu-Ming Peng(彭述明), Shi-Zhong Wei(魏世忠), and Hua-Hai Shen(申华海)
Chin. Phys. B, 2022, 31 (**9**): 096102. DOI: 10.1088/1674-1056/ac6b25

Cluster dynamics modeling of niobium and titanium carbide precipitates in α-Fe and γ-Fe

Nadezda Korepanova, Long Gu(顾龙), Mihai Dima, and Hushan Xu(徐瑚珊)
Chin. Phys. B, 2022, 31 (**2**): 026103. DOI: 10.1088/1674-1056/ac0cd0

Sensitivity of short-range order prediction to machine learning potential formalisms: A case study on NbMoTaW high-entropy alloy

Dingyi Jin(金定毅)[1], Guo Wei(魏国)[2,†], and Haidong Wang(王海东)[3,‡]

[1] *School of Intelligent Manufacturing, Hunan First Normal University, Changsha* 410082, *China*
[2] *Department of Physics and Helsinki Institute of Physics, University of Helsinki, P.O. Box* 43, *Helsinki FI*-00014, *Finland*
[3] *School of Advanced Interdisciplinary Studies, Hunan University of Technology and Business, Changsha* 410082, *China*

(Received 10 July 2025; revised manuscript received 2 September 2025; accepted manuscript online 5 September 2025)

Chemical short-range order (SRO), a phenomenon at the atomic scale resulting from inhomogeneities in the local chemical environment, is usually studied using machine learning force field-based molecular dynamics simulations due to the limitations of experimental methods. To promote the reliable application of machine potentials in high-entropy alloy simulations, first, this work uses NEP models trained on two different datasets to predict the SRO coefficients of NbMoTaW. The results show that within the same machine learning framework, there are significant differences in the prediction of SRO coefficients for the Nb–Nb atomic pair. Subsequently, this work predicts the SRO coefficients of NbMoTaW using the NEP model and the SNAP model, both of which are trained on the same dataset. The results reveal significant discrepancies in SRO predictions for like-element pairs (e.g., Nb–Nb and W–W) between the two potentials, despite the identical training data. The findings of this study indicate that discrepancies in the prediction results of SRO coefficients can arise from either the same machine learning framework trained on different datasets or different learning frameworks trained on the same dataset. This reflects possible incompleteness in the current training set's coverage of local chemical environments at the atomic scale. Future research should establish unified evaluation standards to assess the capability of training sets to accurately describe complex atomic-scale behaviors such as SRO.

Keywords: multi-principal element alloys, short-range order, machine-learning potential

PACS: 61.82.Bg, 75.40.–s, 34.20.Cf

DOI: 10.1088/1674-1056/ae039a **CSTR:** 32038.14.CPB.ae039a

1. Introduction

Elevating the operating temperature of aerospace propulsion systems is essential for optimizing their performance,[1,2] thereby driving the ongoing demand for high-temperature alloy materials. As a subset of multi-principal element alloys, refractory high-entropy alloys (RHEAs) possess significant application potential due to their ability to maintain excellent strength even at working temperatures as high as 1800 °C.[3–5] Among these, the body-centered cubic (BCC) NbMoTaW alloy exhibits a yield strength of approximately 400 MPa at 1600 °C, outperforming the majority of refractory high-entropy alloys and nickel-based superalloys.[6–8] Consequently, the NbMoTaW alloy has gradually emerged as a critical material for manufacturing components in aerospace propulsion systems,[9] owing to its superior mechanical properties under high-temperature, high-pressure, and high-strain-rate conditions. Given that the microstructure of materials significantly influences the mechanical properties of high-entropy alloys,[10] a thorough understanding of the effects of microstructural changes is of great significance for optimizing material performance. Currently, molecular dynamics (MD) simulations have become an important method for studying the microstructural characteristics of materials and their impact on material properties. For example, MD simulations have been widely applied to investigate the nucleation, growth, and coalescence of voids in aluminum under high strain rates;[11] the significant role of load pulse shapes in void evolution and dynamic material damage;[12] the impact-induced deformation and fracture behavior of single-crystalline and nanocrystalline CoCrFeMnNi high-entropy alloys under different impact intensities;[13] and the phase transformation mechanism from BCC to face-centered cubic (FCC) in nanocrystalline CoCrFeMnNi high-entropy alloys under shock loading and its influence on flow stress;[14] the influence of molybdenum (Mo) content on the deformation behavior of γ-phase U–Mo alloys.[15]

The accuracy of MD simulations primarily depends on the precision of the atomic potentials employed.[16] Currently, classical potential functions are commonly used to simulate the physical mechanisms underlying the kinetic behavior of multi-component alloys. However, the simplified treatment of chemical bonding in classical potentials (such as the embedded atom method, EAM) for multi-component systems leads to prediction deviations in key processes, including phase transformations and dislocation migration.[17] To

†Corresponding author. E-mail: weig0307@outlook.com
‡Corresponding author. E-mail: whd@hutb.edu.cn

© 2025 Chinese Physical Society and IOP Publishing Ltd. All rights, including for text and data mining, AI training, and similar technologies, are reserved.

achieve more accurate and efficient simulations of material properties, many researchers have begun to apply artificial intelligence (AI) techniques to material design and simulation. For instance, Xiaoxun Gong *et al.*[18] proposed an efficient real-space reconstruction method that extends deep learning electronic structure calculations from atomic orbital bases to plane-wave bases, thereby enhancing computational efficiency while maintaining high accuracy. Albert Musaelian *et al.*[19] introduced a novel deep neural network architecture named Allegro, which is capable of simulating systems with up to 100 million atoms. Nicolas Bertin *et al.*[20] developed the spectral neighbor analysis potential (SNAP) and utilized it to simulate the crystal plasticity behavior of BCC metal tantalum. Jiuyang Shi *et al.*[25] developed a machine learning potential based on first-principles calculations for high-pressure carbon, demonstrating remarkable performance in simulating the melting process and Hugoniot curve of carbon.

In W-based high-entropy alloys (HEAs), the formation of short-range order (SRO) is attributed to interatomic interactions.[23] This ordering can significantly influence the mechanical properties of the alloy, including strength and ductility.[26] Since SRO is an atomic-scale phenomenon, directly observing its formation and evolution through experiments presents considerable challenges. Many researchers have begun employing machine learning potential functions to investigate the effects of SRO on the properties of high-entropy alloys. For instance, Pedro A. Santos-Florez *et al.*[24] developed a machine learning potential (MLP) based on neural networks and simulated the influence of SRO on the properties of the BCC MoNbTaW multi-principal element alloy (MPEA). Ying Han *et al.*[27] simulated and analyzed the formation mechanism of SRO during the solidification process of the CoCrNi medium-entropy alloy (MEA) and explored its impact on material properties. Le Li *et al.*[28] combined MD simulations with neural network potentials (NNPs) to study the variations in SRO in the equiatomic Cr–Co–Ni MEA under different annealing conditions and their effects on mechanical properties. Fan *et al.*[21] developed a neuroevolution potential (NEP) framework for constructing machine learning potentials based on neural networks. Utilizing the NEP potential model established by Fan *et al.*, Keke Song *et al.*[22] developed a unified machine learning potential model encompassing 16 elements and alloys, validating the model's effectiveness by reproducing the observed chemical ordering and stable phases. Li *et al.*[17] provided a benchmark dataset to train a potential function based on the SNAP model, which analyzed the influence of SRO on the strengthening mechanism of the NbMoTaW alloy.

In this study, given the inherent architectural differences among machine learning potential models, significant variations exist in both simulation accuracy and computational efficiency. To provide guidance for model selection in refractory high-entropy alloy systems, this study first employs NEP models trained on two distinct datasets from Refs. [17,34] to predict the SRO coefficients of NbMoTaW. Subsequently, it utilizes both NEP and SNAP models trained on the same dataset from Ref. [17] to predict the SRO coefficients of NbMoTaW. Furthermore, the work investigates the physical and methodological factors that contribute to the discrepancies in SRO results produced by these distinct models.

2. Methods

2.1. Dataset source

The dataset utilized in this study originates from the training set for the SNAP provided by Li *et al.*[17] The data encompasses a diverse array of structural configurations for niobium (Nb), molybdenum (Mo), tantalum (Ta), and tungsten (W) atoms, including perturbed BCC arrangements and thermodynamically sampled structures. The data labels consist of energy, atomic forces, and stress tensors. In this study, we employed the NEP to train on this standard dataset and compared the training outcomes and SRO prediction results with those obtained using SNAP.

2.2. Introduction to the NEP and SNAP potential models

The NEP is an MLP framework based on neuroevolution strategies. By integrating neural networks with evolutionary algorithms, NEP attains a high level of accuracy and efficiency in atomic-scale simulations.[21] In contrast to conventional empirical potentials, NEP maintains near first-principles accuracy while achieving computational speeds comparable to those of empirical potentials, making it suitable for large-scale simulations of complex materials (such as phase transformations, radiation damage, and mechanical behavior). A brief introduction to the training procedure for NEP is provided below.[29]

(i) Dataset construction Reference data are generated through first-principles calculations (such as density functional theory, DFT), covering various phases (crystalline, amorphous, liquid, interfaces, etc.), defect structures, and configurations under extreme conditions (high pressure, high temperature) of the target materials. Generally, the dataset is divided into training and testing sets in a 90% to 10% ratio. This division is implemented to ensure that the error observed in the testing set closely approximates that of the training set, thereby mitigating the risk of overfitting.

(ii) Descriptor construction The NEP model describes the local chemical environment of atom i using a descriptor vector $\boldsymbol{q}_i$. The descriptor consists of both radial and angular components, which are used to encode information about the local atomic environment.

The radial descriptor q_n^i serves to characterize the spatial distribution of distances between an atom and its neighboring atoms. This descriptor is based on the distance r_{ij} between atomic pairs and takes the form

$$q_n^i = \sum_{j\neq i} g_n(r_{ij}). \tag{1}$$

Here, the term $g_n(r_{ij})$ denotes the local chemical environment characteristic associated with the interatomic distance r_{ij} between atoms i and j. It characterizes the intricate patterns of varying atomic distances via a linear combination of basis functions $f_k(r_{ij})$ and expansion coefficients c_{nk}^{IJ}, as illustrated in the subsequent expression:

$$g_n(r_{ij}) = \sum_{k=0}^{N_{\text{bas}}^R} c_{nk}^{IJ} f_k(r_{ij}), \tag{2}$$

where $f_k(r_{ij})$ represents the Chebyshev basis functions with a cutoff distance. The variable N_{bas}^R denotes the total number of basis functions (i.e., the maximum value of k), which influences the complexity of the descriptor. The expansion coefficients c_{nk}^{IJ} indicate the contribution weights of the k-th basis function to the n-th radial descriptor. The superscripts I and J signify the types of chemical elements associated with the central atom i and the neighboring atom j, respectively, thereby illustrating the variations in interactions among different pairs of elements. These coefficients can be optimized through machine learning. In summary, the radial descriptor depends solely on the interatomic distance r_{ij} and inherently exhibits translational and rotational invariance.

The angular descriptor q_{nl}^i characterizes many-body interactions, encompassing terms related to three-body, four-body, and five-body interactions. The formulation for the three-body interaction is as follows:

$$q_{nl}^i = \frac{2l+1}{4\pi} \sum_{j\neq i} \sum_{k\neq i} g_n(r_{ij}) g_n(r_{ik}) P_l\left(\cos\theta_{ijk}\right). \tag{3}$$

Here, the term q_{nl}^i refers to the three-body angular descriptor component for the i-th atom, which is jointly indexed by the angular quantum number l and the radial basis function index n. The term $g_n(r_{ij})$ characterizes the local chemical environment based on the interatomic distance r_{ij} between atoms i and j. $P_l(\cos\theta_{ijk})$ is the Legendre polynomial, where the parameter $\cos\theta_{ijk}$ is the cosine of the angle between vectors $\boldsymbol{ij}$ and $\boldsymbol{ik}$. This polynomial ensures the invariance of the descriptor under rotation, translation, and atomic permutation. The normalization coefficient $\frac{2l+1}{4\pi}$ is included to further ensure the rotational invariance of the descriptor.

The incorporation of the spherical harmonics $Y_{lm}(\theta_{ij}, \phi_{ij})$ facilitates the transformation of the angular descriptor q_{nl}^i into a more computationally efficient form, as shown below:

$$q_{nl}^i = \sum_{m=-l}^{l} \left|A_{nlm}^i\right|^2, \tag{4}$$

where $A_{nlm}^i = \sum_{j\neq i} g_n(ij) Y_{lm}(\theta_{ij}, \phi_{ij})$, the summation form ensures that the angular descriptor q_{nl}^i remains invariant under rotation operations.

The descriptors of the NEP model are formulated utilizing Chebyshev and Legendre polynomials, as well as spherical harmonics, for the radial and angular components. This approach inherently accommodates translational, rotational, and permutational symmetries.

(iii) Construction of neural network models The NEP model employs a single-hidden-layer feedforward neural network (feedforward neural network, FNN) as the core architecture of the machine learning model. This network configuration consists of an input layer, a solitary hidden layer, and an output layer.

The input layer is responsible for receiving the descriptor vector $\boldsymbol{q}_i$ associated with atom i, which encodes its local chemical environment. Each neuron within the hidden layer processes the weighted input derived from the descriptor vector $\boldsymbol{q}_i$, as expressed by

$$\sum_{\nu=1}^{N_{\text{des}}} w_{\mu\nu}^0 q^i - b_\mu^0. \tag{5}$$

Subsequently, the activation function tanh is employed to generate nonlinear features, as represented by the following mathematical expression:

$$\tanh\left(\sum_{\nu=1}^{N_{\text{des}}} w_{\mu\nu}^0 q^i - b_\mu^0\right). \tag{6}$$

The output layer then calculates the weighted sum of outputs from the hidden layer and incorporates a global bias b^1, resulting in the determination of the site energy U_i for atom i. The calculation is given by the following formula:

$$U_i = \sum_{\mu=1}^{N_{\text{neu}}} w_\mu \tanh\left(\sum_{\nu=1}^{N_{\text{des}}} w_{\mu\nu}^0 q^i - b_\mu^0\right) - b^1. \tag{7}$$

Within the framework of the NEP model, the neural network serves as a universal function approximator, mapping symmetric descriptors to corresponding symmetric energy outputs.

(iv) Loss function design The NEP model employs a comprehensive loss function design, optimizing model performance by combining the error terms of multiple key physical quantities through weighted summation.

(v) Design of the training algorithm The NEP model employs the separable natural evolution strategy (SNES) for parameter optimization, which is an efficient evolutionary algorithm particularly suited for optimization problems in high-dimensional parameter spaces.

(vi) Hyperparameter setting The hyperparameters of the NEP model are set through the configuration file nep.in.

The SNAP is an interatomic potential model grounded in machine learning principles, which characterizes the local atomic environment through the utilization of bispectrum components. This model incorporates four-dimensional hyperspherical harmonics to expand the density function of neighboring atoms, ensuring compliance with the principles of

rotational and translational invariance. The detailed methodology is outlined as follows.[30]

(i) Description of the local atomic environment SNAP describes the atomic neighborhood density by projecting it onto a four-dimensional hypersphere. The function representing neighborhood density is defined as follows:

$$\rho_i = \delta(r) + \sum_{r_{ii'}<R_{\rm cut}} f_{\rm c}(r_{ii'}) w_{i'} \delta(r - r_{ii'}), \tag{8}$$

where $\delta(r)$ represents the density contribution of the central atom i itself, expressed as a three-dimensional Dirac function. Its physical meaning is that there exists a point-like density distribution at the location of the central atom i; $r_{ii'}$ denotes the position vector connecting atom i and its neighboring atom i'; $f_{\rm c}(r_{ii'})$ is a smooth cutoff function; $w_{i'}$ represents the atomic type weight, which is utilized to differentiate between various chemical elements; the summation term accounts for the density contributions from neighboring atoms i' that fall within the specified cutoff range $R_{\rm cut}$ relative to the central atom i.

(ii) Expansion in four-dimensional hyperspherical harmonics First, establish the mapping relationship between the distance r in three-dimensional space between the central atom and its neighboring atoms and the latitude angle θ_0 on the four-dimensional hypersphere:

$$\theta_0 = \theta_0^{\max} \frac{r}{R_{\rm cut}}, \tag{9}$$

where θ_0 is the latitude angle on the four-dimensional hypersphere ($0 \le \theta_0 \le \theta_0^{\max}$); and $\theta_0^{\max}$ is the maximum latitude angle for the mapping.

Then, the density function defined on the 3-sphere is expanded as a linear combination of the four-dimensional hyperspherical harmonics $U^j_{m,m'}(\theta_0,\theta,\phi)$, with its specific form given as follows:

$$\rho(r) = \sum_{j=0,\frac{1}{2},\ldots}^{\infty} \sum_{m=-j}^{j} \sum_{m'=-j}^{j} u^j_{m,m'} U^j_{m,m'}(\theta_0,\theta,\phi). \tag{10}$$

Here, j represents the total angular momentum quantum number; m and m' denote projection quantum numbers; $u^j_{m,m'}$ is the expansion coefficient, and its calculation formula is provided as follows:

$$\begin{aligned} u^j_{m,m'} &= U^j_{m,m'}(0,0,0) \\ &\quad + \sum_{r_{ii'}<R_{\rm cut}} f_{\rm c}(r_{ii'}) w_{i'} U^j_{m,m'}(\theta_0,\theta,\phi), \end{aligned} \tag{11}$$

where $U^j_{m,m'}(0,0,0)$ describes the central atom's own contribution; the summation term represents the contributions of all neighboring atoms i', with the weight determined by the cutoff function $f_{\rm c}(r_{ii'})$ and the atomic type weight $w_{i'}$.

(iii) Construct the bispectrum components The bispectrum component $B_{j_1,j_2,j}$ transforms the expansion coefficients $u^j_{m,m'}$ of the four-dimensional hyperspherical harmonics $U^j_{m,m'}(\theta_0,\theta,\phi)$ into rotationally invariant quantities via triple coupling, and is used to characterize the rotationally invariant features of the local atomic environment. The specific form of the formula is as follows:

$$\begin{aligned} B_{j_1,j_2,j} &= \sum_{m_1,m_1'=-j_1}^{j_1} \sum_{m_2,m_2'=-j_2}^{j_2} \sum_{m,m'=-j}^{j} \left(u^j_{m,m'}\right) \\ &\quad \times H \begin{matrix} jmm' \\ j_1 m_1 m_1' \\ j_2 m_2 m_2' \end{matrix} u^{j_1}_{m_1,m_1'} u^{j_2}_{m_2,m_2'}, \end{aligned} \tag{12}$$

where $H \begin{matrix} jmm' \\ j_1 m_1 m_1' \\ j_2 m_2 m_2' \end{matrix}$ is a coupling coefficient, which converts the basis functions associated with various angular momenta (j_1, j_2, j) into scalar invariants through coupling.

The bispectrum component $B_{j_1,j_2,j}$ exhibits the following symmetry relations under the exchange of the angular momentum quantum numbers j_1, j_2, j:

$$\frac{B_{j_1,j_2,j}}{2j+1} = \frac{B_{j,j_2,j_1}}{2j_1+1} = \frac{B_{j_1,j,j_2}}{2j_2+1}.$$

The above symmetry relations exhibit rotational invariance and permutation symmetry.

The potential energy of the SNAP model decomposes the total energy of the system into reference energy and local energy

$$E\left(r^N\right) = E_{\rm ref}\left(r^N\right) + E_{\rm loacl}\left(r^N\right). \tag{13}$$

Here, $E_{\rm ref}\left(r^N\right)$ is the reference energy, which describes global physical phenomena such as long-range electrostatic interactions (e.g., interionic Coulomb forces), and is generally based on well-established analytical models; the local energy $E_{\rm loacl}\left(r^N\right)$ accounts for additional effects that are not encompassed by the reference energy.

The local energy $E_{\rm loacl}\left(r^N\right)$ in SNAP is assumed to have a linear relationship between its atomic energy and the bispectrum components, with its expression given as follows:

$$E_{\rm loacl}\left(r^N\right) = N\beta_0 + \boldsymbol{\beta} \cdot \sum_{i=1}^{N} \boldsymbol{B}^i, \tag{14}$$

where N is the total number of atoms in the system; β_0 denotes the constant energy term (ground state energy) for each atom, which is independent of atomic type; $\boldsymbol{\beta}$ is the SNAP coefficient vector, determined by fitting to quantum mechanical data via linear regression; $\boldsymbol{B}^i$ is the K-vector of bispectrum components for atom i, describing the symmetry-invariant features of its local environment and ensuring that energy calculations are independent of the coordinate system.

It can be inferred from the preceding discussion that the descriptors of the NEP model construct radial and angular components utilizing Chebyshev and Legendre polynomials, as well as spherical harmonics, thereby inherently fulfilling

translational, rotational, and permutational symmetries. In contrast, the SNAP model accomplishes the characterization of these symmetries through the use of bispectrum components.

3. Simulation methods and SRO calculations

Initially, the NEP model was trained utilizing a standard dataset from Ref. [17], employing four A10 GPUs, a process that required approximately four days to finalize. The specifics of the nep.in utilized in this research are presented as follows:

type	4	Nb Mo Ta W
version	4	
cutoff	6	4
n_max	8	8
basis_size	12	8
l_max	4	2 0
neuron	80	
lambda_1	0.2	
lambda_2	0.2	
lambda_e	1	
lambda_f	1	
lambda_v	0.1	
batch	10000	
population	60	
generation	3000000	

Subsequently, the trained NEP potential was utilized to perform Monte Carlo/molecular dynamics (MC/MD) simulations employing the GPUMD software.[31–33] The single-crystal model was designed with dimensions of $15.5 \times 15.5 \times 15.5$ nm^3 ($48 \times 48 \times 48$ conventional unit cells), with all atoms randomly distributed. The simulations were conducted, and the temperature was maintained at room temperature (300 K), with a time step of 5 fs, which is the same as that in Ref. [17]. The total duration of the simulation was 15 ns, which was deemed sufficient to achieve thermodynamic equilibrium. The NPT ensemble (constant temperature and pressure) was used, with the pressure set to 0. Periodic boundary conditions were applied in all three dimensions. To ensure the statistical reliability of MC/MD simulations, five independent repeats were performed using five different random seeds, with each simulation lasting 15 ns. To analyze the influence of initial structures on the simulated results, three distinct initial configurations were employed for MC/MD simulations, with each simulation also running for 15 ns. Finally, a NbMoTaW solid-solution model was constructed to calculate the distribution probabilities of various elemental pairs within the coordination shells, and the Warren–Cowley parameters were used to quantify the short-range order.

In this study, the formulas utilized for calculating the Warren–Cowley parameters are derived from Refs. [17,26], respectively:

$$\mathrm{WCP}_{ij} = 1 - \frac{Z_{ij}}{\chi_j Z_i}. \tag{15}$$

Equation (15) referenced in Ref. [26], where WCP_{ij} is the Warren–Cowley short-range order parameter for ij atomic pairs. This parameter is used to quantify the degree of chemical segregation between i-type and j-type atoms within the first nearest-neighbor shell. Specifically, a negative value indicates a clustering tendency of atomic pairs, reflecting an ordering trend; conversely, a positive value suggests a preferential segregation tendency, indicative of disorder. A value of zero corresponds to a random distribution of atoms. Here, Z_{ij} represents the actual observed number of j-type atoms in the first nearest-neighbor shell surrounding i-type atoms; Z_i denotes the total number of first nearest neighbors of i-type atoms; χ_j signifies the atomic fraction (concentration) of j-type atoms in the alloy. When $\mathrm{WCP}_{ij} > 0$, it reflects preferential segregation between the two types of atoms; when $\mathrm{WCP}_{ij} < 0$, it implies a tendency toward atomic ordering. The following equation is derived from Ref. [17]:

$$a_{ij}^k = \frac{p_{ij}^k - c_j}{\delta_{ij} - c_j}, \tag{16}$$

where a_{ij}^k is the chemical SRO parameter for the k-th nearest-neighbor shell; p_{ij}^k represents the average probability of locating j-type atoms within the k-th shell; c_j denotes the average concentration of j-type atoms throughout the system; δ_{ij} is the Kronecker delta function (equal to 1 when $i = j$, and 0 otherwise). For identical atomic pairs (i.e., $i = j$), a positive a_{ij}^k indicates a tendency toward atomic ordering between the two types of atoms within the k-th coordination shell, whereas a negative value suggests a preference for preferential segregation. By contrast, for distinct atomic pairs (i.e., $i \neq j$), the interpretation reverses: a negative a_{ij}^k signifies a propensity for clustering of j-type atoms within the k-th coordination shell of i-type atoms, while a positive value denotes a preferential segregation tendency between the two types of atoms.

4. Results and discussion

4.1. Assessment of the training quality of the NEP potential

The NEP potential constructed in this study was assessed for accuracy in terms of energy and force within both the training and test datasets provided by Li *et al.*[17] The results are shown in Fig. 1: the mean absolute error (MAE) of energy for the training set is 1.106 meV/atom, and that for the test set is 1.45 meV/atom; the MAE of force for the training set is 0.080569 eV/Å, and the MAE of force for the test set is 0.136557 eV/Å. For the literature data in Ref. [17], the MAE

of energy for the training set is 4.3 meV/atom, and that for the test set is 5.1 meV/atom; the MAE of force for the training set is 0.13 eV/Å, and the MAE of force for the test set is 0.14 eV/Å. The comparison of the above training results suggests that the NEP model, constructed using the standard dataset, demonstrates superior training performance relative to the SNAP model, which was also developed using the same standard dataset.

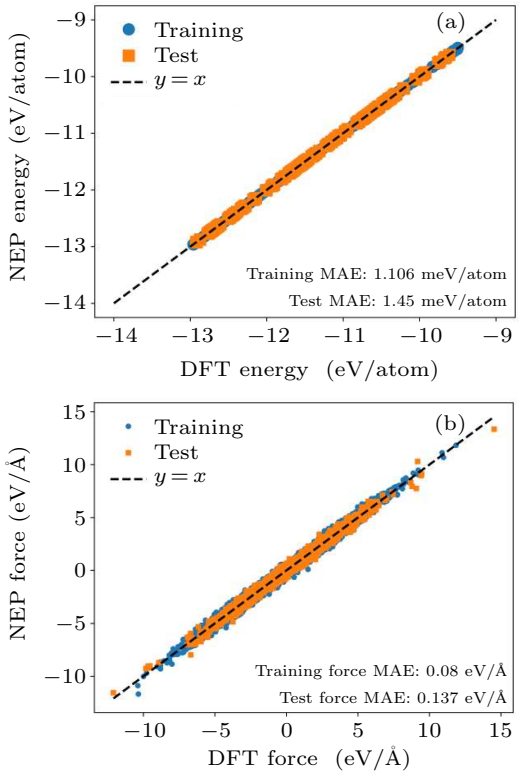


Fig. 1. Performance of the NEP model in predicting energies and forces.

4.2. Comparison results of SRO

The quaternary NbMoTaW multi-principal element alloy model adopted in this study is illustrated in Fig. 2. Figure 3 presents the energy variation curve derived from simulations conducted using the NEP model, plotted against the iteration number (time) of the MC/MD simulations. The results show that as the simulation duration extends, the energy exhibits a gradual stabilization, suggesting that the NEP model developed in this study progressively converges with the increase of simulation time.

In this study, equations (15) and (16) were employed to compute the temporal variations of the SRO coefficients in the first neighboring layer. The temporal evolution of the first-nearest-neighbor SRO coefficients under different initial seeds and different initial structures is shown in Figs. 4 and 5, respectively. The results demonstrate that the error bars of the first-nearest-neighbor SRO coefficients predicted by the NEP model trained in this work and the NEP model trained by Liu *et al.*[34] gradually decrease over time. Combined with the above findings, it can be concluded that the simulation results in this study are minimally influenced by initial seeds and initial structures. Therefore, the average values of the SRO coefficients are adopted as the final predictions. A comparison of the predicted values from the NEP model trained in this work, the NEP model from Ref. [34], and the SNAP model[17] under different initial seeds is summarized in Table 1. The comparative results based on different initial structures are presented in Table 2.

As indicated by the results in Tables 1 and 2, under different initial seeds and initial structural configurations, the predicted SRO coefficients for heterotypic element pairs show substantial consistency between the NEP model trained in this work and the NEP model from Ref. [34]. However, discrepancies are observed in the predicted SRO coefficients for the homotypic Nb–Nb element pair between these two models. Notably, the NEP model developed in this work and the SNAP model — both trained on the same dataset from Ref. [17] — exhibit opposite trends in predicting the SRO coefficients for homotypic Nb–Nb and W–W element pairs.

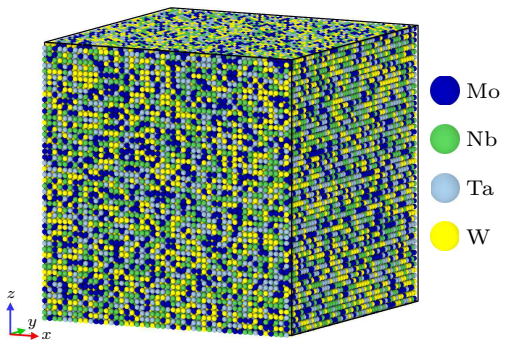


Fig. 2. Atomic configuration of a random solid solution model of a quaternary alloy. Dark blue, green, light blue, and yellow spheres represent Mo, Nb, Ta, and W atoms, respectively.

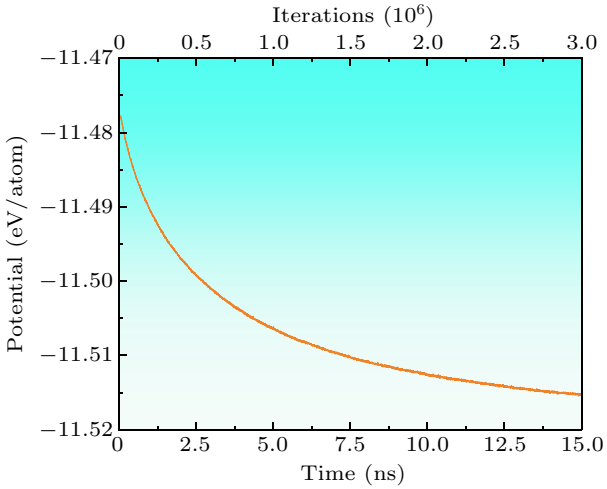


Fig. 3. Curve of system energy versus iteration number (time) in MC/MD simulations.

Table 1. Under different initial seeds for MC/MD simulations: Comparison of the predicted average SRO coefficients among the NEP model trained in this work, the NEP model by Liu *et al.*,[34] and the SNAP model.[17] (S: segregation, O: ordering)

Pairs	By SNAP[17]	By NEP using Eq. (15)	By NEP using Eq. (16)	By NEP[Liu *et al.*] using Eq. (15)	By NEP[Liu *et al.*] using Eq. (16)
Mo–Mo	−0.19 (S)	0.900 ± 0.001 (S)	−0.299 ± 0.001 (S)	0.882 ± 0.002 (S)	−0.294 ± 0.001 (S)
Mo–Nb	−0.33 (O)	−0.441 ± 0.002 (O)	−0.441 ± 0.002 (O)	−0.359 ± 0.004 (O)	−0.359 ± 0.003 (O)
Mo–Ta	−0.51 (O)	−1.086 ± 0.001 (O)	−1.09 ± 0.001 (O)	−1.016 ± 0.003 (O)	−1.02 ± 0.003 (O)
Mo–W	0.28 (S)	0.629 ± 0.002 (S)	0.629 ± 0.002 (S)	0.493 ± 0.004 (S)	0.493 ± 0.004 (S)
Nb–Nb	−0.01 (S)	−0.069 ± 0.002 (O)	0.023 ± 0.001 (O)	0.073 ± 0.004 (S)	−0.024 ± 0.001 (S)
Nb–Ta	0.36 (S)	0.569 ± 0.002 (S)	0.569 ± 0.002 (S)	0.482 ± 0.003 (S)	0.482 ± 0.003 (S)
Nb–W	−0.05 (O)	−0.065 ± 0.002 (O)	−0.065 ± 0.002 (O)	−0.205 ± 0.002 (O)	−0.205 ± 0.002 (O)
Ta–Ta	−0.16 (S)	0.738 ± 0.002 (S)	−0.246 ± 0.001 (S)	0.700 ± 0.003 (S)	−0.233 ± 0.001 (S)
Ta–W	−0.34 (O)	−0.249 ± 0.001 (O)	−0.249 ± 0.001 (O)	−0.196 ± 0.003 (O)	−0.195 ± 0.003 (O)
W–W	−0.04 (S)	−0.308 ± 0.002 (O)	0.102 ± 0.001 (O)	−0.083 ± 0.003 (O)	0.028 ± 0.001 (O)

Table 2. Under different initial structural configurations: Comparison of the predicted average SRO coefficients among the NEP model trained in this work, the NEP model by Liu *et al.*,[34] and the SNAP model.[17] (S: segregation, O: ordering)

Pairs	By SNAP[17]	By NEP using Eq. (15)	By NEP using Eq. (16)	By NEP[Liu *et al.*] using Eq. (15)	By NEP[Liu *et al.*] using Eq. (16)
Mo–Mo	−0.19 (S)	0.901 ± 0.002 (S)	−0.300 ± 0.001 (S)	0.883 ± 0.002 (S)	−0.294 ± 0.001 (S)
Mo–Nb	−0.33 (O)	−0.445 ± 0.003 (O)	−0.445 ± 0.003 (O)	−0.360 ± 0.003 (O)	−0.360 ± 0.003 (O)
Mo–Ta	−0.51 (O)	−1.087 ± 0.003 (O)	−1.087 ± 0.003 (O)	−1.023 ± 0.003 (O)	−1.02 ± 0.003 (O)
Mo–W	0.28 (S)	0.632 ± 0.002 (S)	0.632 ± 0.002 (S)	0.494 ± 0.003 (S)	0.494 ± 0.003 (S)
Nb–Nb	−0.01 (S)	−0.068 ± 0.001 (O)	0.022 ± 0.001 (O)	0.071 ± 0.004 (S)	−0.024 ± 0.001 (S)
Nb–Ta	0.36 (S)	0.570 ± 0.002 (S)	0.570 ± 0.002(S)	0.484 ± 0.002 (S)	0.484 ± 0.002 (S)
Nb–W	−0.05 (O)	−0.064 ± 0.001 (O)	−0.064 ± 0.001 (O)	−0.205 ± 0.001 (O)	−0.205 ± 0.001 (O)
Ta–Ta	−0.16 (S)	0.740 ± 0.004 (S)	−0.247 ± 0.001 (S)	0.702 ± 0.002 (S)	−0.234 ± 0.001 (S)
Ta–W	−0.34 (O)	−0.250 ± 0.001 (O)	−0.250 ± 0.001 (O)	−0.199 ± 0.003 (O)	−0.199 ± 0.003 (O)
W–W	−0.04 (S)	−0.311 ± 0.001 (O)	0.104 ± 0.001 (O)	−0.081 ± 0.004 (O)	0.027 ± 0.001 (O)

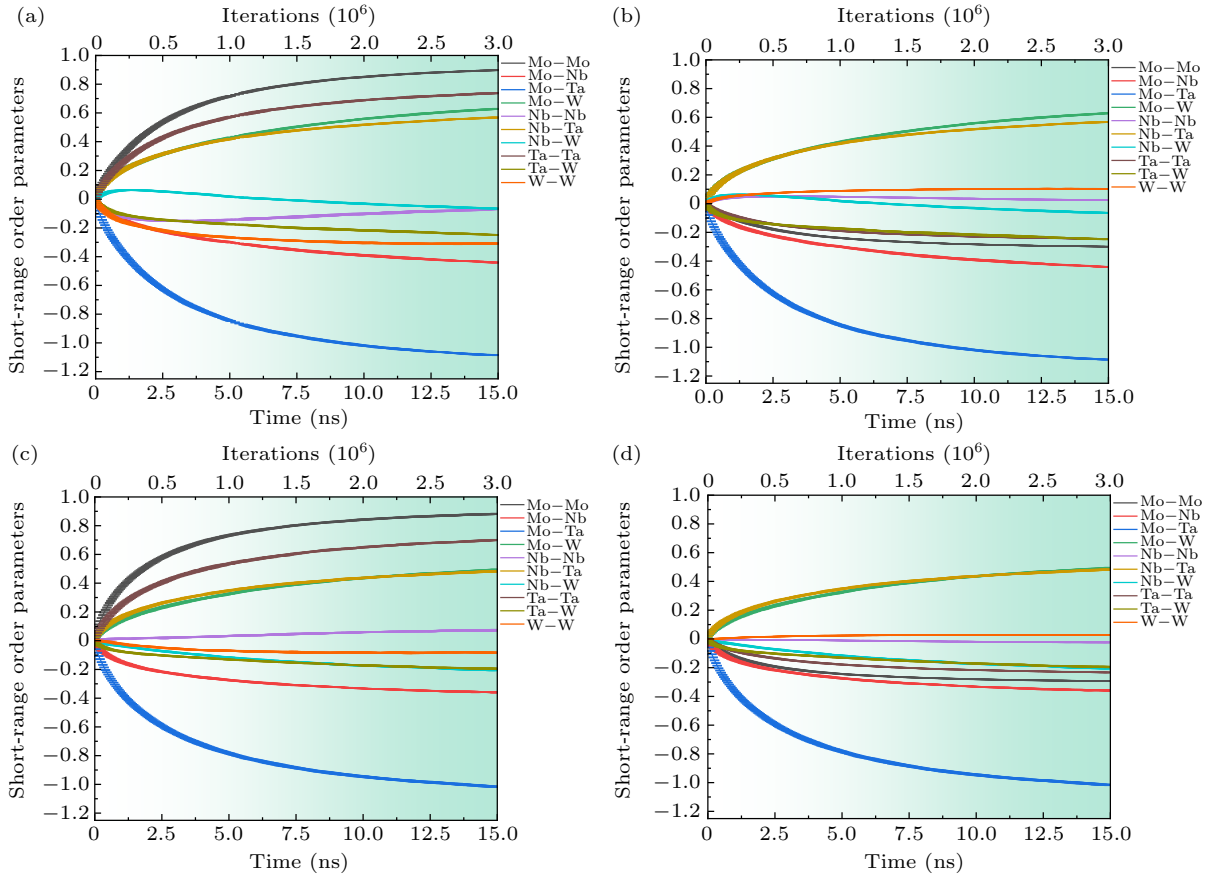


Fig. 4. Under different initial seeds for MC/MD simulations: (a) temporal evolution of the first-nearest-neighbor SRO coefficients calculated using Eq. (15) for the NEP model trained in this work; (b) temporal evolution of the first-nearest-neighbor SRO coefficients calculated using Eq. (16) for the NEP model trained in this work; (c) temporal evolution of the first-nearest-neighbor SRO coefficients calculated using Eq. (15) for the NEP model trained by Liu *et al.*;[34] (d) temporal evolution of the first-nearest-neighbor SRO coefficients calculated using Eq. (16) for the NEP model trained by Liu *et al.*[34]

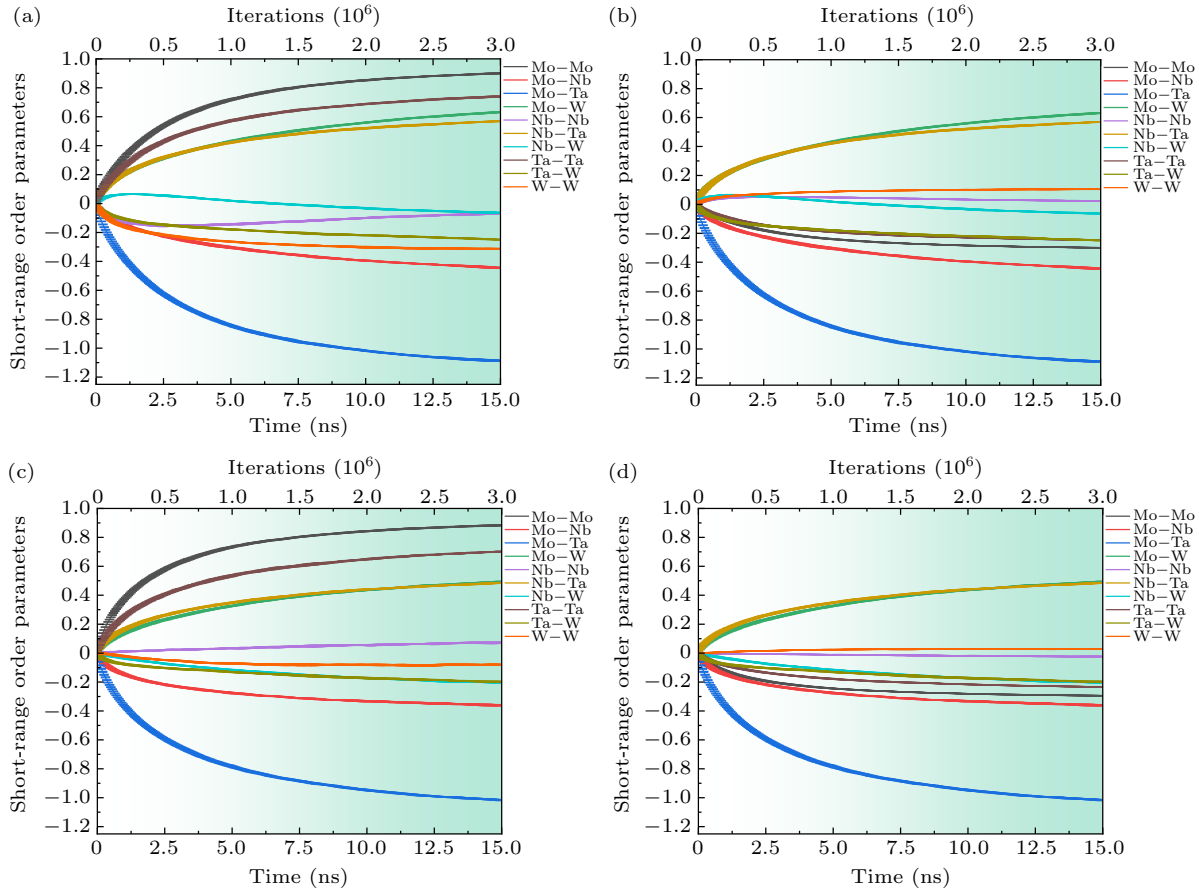


Fig. 5. Under different initial structural configurations: (a) temporal evolution of the first-nearest-neighbor SRO coefficients calculated using Eq. (15) for the NEP model trained in this work; (b) temporal evolution of the first-nearest-neighbor SRO coefficients calculated using Eq. (16) for the NEP model trained in this work; (c) temporal evolution of the first-nearest-neighbor SRO coefficients calculated using Eq. (16) for the NEP model trained by Liu *et al.*;[34] (d) temporal evolution of the first-nearest-neighbor SRO coefficients calculated using Eq. (16) for the NEP model trained by Liu *et al.*[34]

4.3. Discussion

The above results indicate that the NEP models trained on different datasets exhibit significant differences in the predicted SRO coefficients for the Nb–Nb element pair. In contrast, the NEP model and the SNAP model trained on the same dataset show notable discrepancies in the predicted SRO coefficients for both W–W and Nb–Nb pairs. The NEP model from Ref. [34] uses a cutoff radius of 5 Å for both its radial and angular descriptor components. In comparison, the NEP model developed in this work employs cutoff radii of 6 Å and 4 Å for the radial and angular descriptors, respectively. Additionally, the training datasets used for the NEP models originate from Refs. [17,34], which are distinct datasets. This suggests that variations in both hyperparameters (such as cutoff radii) and training datasets may lead to differences in SRO predictions. Although the comparative results imply that both hyperparameters and training datasets could influence SRO predictions, it remains challenging to quantitatively separate their individual contributions. This issue warrants further controlled variable analysis after standardizing the evaluation criteria for training datasets.

The NEP model utilized in this research employs descriptors that construct radial and angular components through Chebyshev and Legendre polynomials, as well as spherical harmonics, thereby inherently satisfying the symmetries of translation, rotation, and permutation. In contrast, the SNAP model, which is predicated on bispectrum components, expands the atomic neighbor density function using four-dimensional hyperspherical harmonics and captures symmetry through these bispectrum components. The NbMoTaW high-entropy alloy possesses a body-centered cubic (BCC) structure characterized by structural symmetry, and both the SNAP and NEP models are capable of effectively representing the symmetry inherent in the BCC structure.

The SRO in high-entropy alloys is a complex atomic-scale phenomenon that arises from the inhomogeneity of the local chemical environment and is intricately linked to the types and properties of the constituent elements.[27] Nevertheless, existing experimental methodologies continue to face challenges in precisely characterizing the features of SRO and determining the critical thresholds that distinguish order from disorder for validation purposes.[27,35] Therefore, limited by experimental capabilities, there remains an absence of a definitive standard to ascertain whether the training dataset ade-

quately represents all potential local chemical environments relevant to the subject of investigation.

5. Conclusion

This work systematically compares the predictive performance of NEP models trained on different datasets, as well as that of NEP and SNAP models trained on the same dataset, regarding the SRO coefficients of the NbMoTaW alloy. The predicted first-nearest-neighbor SRO coefficients for Nb–Nb pairs from the NEP models trained on different datasets exhibit opposite trends. These findings indicate that employing different training datasets within the same machine learning framework can lead to divergent learning outcomes. Furthermore, significant discrepancies are observed between the NEP model and the SNAP model — trained on the same dataset — in their predicted SRO coefficients for both W–W and Nb–Nb pairs. This suggests that different machine learning frameworks may yield varying results even when learning from identical training data. Our results imply that current training datasets may not comprehensively encompass all possible local chemical environments at the atomic scale. In practical applications, this limitation in training data could lead to potential-dependent variations in structural predictions. Therefore, it is necessary to establish unified evaluation standards in the future to assess the capability of training datasets in describing complex atomic-scale behaviors, such as SRO, and to promote the reliable application of interatomic potentials in simulating complex systems like high-entropy alloys.

Acknowledgment

Project supported by the Hunan Provincial Natural Science Foundation (Grant Nos. 2024JJ6190 and 2024JK2007-1).

References

[1] Ritchie R O and Zheng X R 2022 *Nat. Mater.* **21** 968
[2] Ritchie R O 2011 *Nat. Mater.* **10** 817
[3] Belcher C H, MacDonald B E, Apelian D and Lavernia E J 2023 *Prog. Mater. Sci.* **137** 101140
[4] Miracle D B and Senkov O N 2017 *Acta Mater.* **122** 448
[5] George E P, Raabe D and Ritchie R O 2019 *Nat. Rev. Mater.* **4** 515
[6] Senkov O N, Wilks G B, Scott J M and Miracle D B 2011 *Intermetallics* **19** 698
[7] Kumar P, Kim S J, Yu Q, Ell J, Zhang M, Yang Y, Kim J Y, Park H K, Minor A M, Park E S and Ritchie R O 2023 *Acta Mater.* **245** 118620
[8] Senkov O N, Miracle D B, Chaput K J and Couzinie J P 2018 *J. Mater. Res.* **33** 3092
[9] George E P, Curtin W A and Tasan C C 2020 *Acta Mater.* **188** 435
[10] Trivedi P B, Asay J R, Gupta Y M and Field D P 2007 *J. Appl. Phys.* **102** 83513
[11] Yang X, Zeng X, Wang J, Wang J, Wang F and Ding J 2019 *Mech. Mater.* **135** 98
[12] Zhu Y, Hu J, Wei Q, Zhang J, Sun Y, Luo G and Shen Q 2023 *Mech. Mater.* **186** 104809
[13] Li W, Chen S, Aitken Z and Zhang Y W 2023 *Int. J. Plast.* **168** 103691
[14] Li W, Xiang M, Aitken Z H, Chen S, Xu Y, Yang X, Pei Q, Wang J, Li X, Vastola G, Gao H and Zhang Y W 2024 *Int. J. Plast.* **178** 104010
[15] Wang C, Peng Peng and Lai W S *Chin. Phys. B* **34** 18101
[16] Frank J T, Unke O T, Müller K R and Chmiela S 2024 *Nat. Commun.* **15** 6539
[17] Li X G, Chen C, Zheng H, Zuo Y and Ong S P 2020 *npj Comput. Mater.* **6** 70
[18] Gong X, Louie S G, Duan W and Xu Y 2024 *Nat. Comput. Sci.* **4** 752
[19] Musaelian A, Batzner S, Johansson A, Sun L, Owen C J, Kornbluth M and Kozinsky B 2023 *Nat. Commun.* **14** 579
[20] Bertin N, Carson R, Bulatov V V, Lind J and Nelms M 2023 *Acta Mater.* **260** 119336
[21] Fan Z, Zeng Z, Zhang C, Wang Y, Song K, Dong H, Chen Y and Ala-Nissila T 2021 *Phys. Rev. B* **104** 104309
[22] Song K, Zhao R, Liu J, Wang Y, Lindgren E, Wang Y, Chen S, Xu K, Liang T, Ying P, Xu N, Zhao Z, Shi J, Wang J, Lyu S, Zeng Z, Liang S, Dong H, Sun L, Chen Y, Zhang Z, Guo W, Qian P, Sun J, Erhart P, Ala-Nissila T, Su Y and Fan Z 2024 *Nat. Commun.* **15** 10208
[23] Fisher J C 1954 *Acta Metall.* **2** 9
[24] Santos-Florez P A, Dai S C, Yao Y, Yanxon H, Li L, Wang Y J, Zhu Q and Yu X X 2023 *Acta Mater.* **255** 11904
[25] Shi J, Liang Z, Wang J, Pan S, Ding C, Wang Y, Wang H T, Xing D and Sun J 2023 *Phys. Rev. Lett.* **131** 146101
[26] Chen S, Aitken Z H, Pattamatta S, Wu Z, Yu Z G, Srolovitz D J, Liaw P K and Zhang Y W 2021 *Nat. Commun.* **12** 4953
[27] Han Y, Chen H, Sun Y, Liu J, Wei S, Xie B, Zhang Z, Zhu Y, Li M, Yang J, Chen W, Cao P and Yang Y 2024 *Nat. Commun.* **15** 6486
[28] Li L, Du J P, Ogata S and Inui H 2024 *Acta Mater.* **269** 119775
[29] Ying P, Qian C, Zhao R, Wang Y, Xu K, Ding F, Chen S and Fan Z 2025 *Chem. Phys. Rev.* **6** 11310
[30] Thompson A P, Swiler L P, Trott C R, Foiles S M and Tucker G J 2015 *J. Comput. Phys.* **285** 316
[31] Fan Z, Wang Y, Ying P, Song K, Wang J, Wang Y, Zeng Z, Xu K, Lindgren E, Rahm J M, Gabourie A J, Liu J, Dong H, Wu J, Chen Y, Zhong Z, Sun J, Erhart P, Su Y and Ala-Nissila T 2022 *J. Chem. Phys.* **157** 114801
[32] Song K, Liu J, Chen S, Fan Z, Su Y and Qian P 2024 arXiv:2404.13694 [cond-mat.mtrl-sci]
[33] Xu K, Bu H, Pan S, *et al.* 2025 *Mater. Genome Eng. Adv.* **3** e70028
[34] Liu J, Byggmästar J, Fan Z, Bai B, Qian P and Su Y 2025 *J. Nucl. Mater.* **616** 156004
[35] Pei Z, Zhang X, Eisenbach M and Liaw P K 2025 *Acta Mater.* **286** 120713